CMS Physics Analysis Summary

Electromagnetic calorimeter commissioning and first results with 7 TeV data

The CMS Collaboration

Abstract

The operation and general performance of the CMS electromagnetic calorimeter at $\sqrt{s} = 7$ TeV are described. The first LHC beams have been used to finalize the commissioning of ECAL readout and trigger and to verify the readiness of ECAL for data taking.

1 Introduction

This article describes how the data collected in the first few months of LHC operation at $\sqrt{s} = 7$ TeV have been used to verify and improve the performance of the electromagnetic calorimeter (ECAL) of CMS and be ready for extended operation throughout 2010 and 2011. Improvements have been made in areas such as timing, trigger efficiency and reconstruction. Detailed comparisons with simulation have been made and show an excellent understanding of the detector.

A complete description of the CMS experiment can be found in [1]. The ECAL comprises a barrel ("EB") and two endcaps ("EE") based on lead tungstate ($PbWO_4$) scintillating crystals, with a silicon-strip preshower ("ES") in front of each EE. EB coverage is to $\eta = 1.479$ with the EE extending to $\eta = 3.0$. The ES covers $1.653 < \eta < 2.6$. Energy measurements from the individual crystals in the EB and EE are supplemented by independent readout of sums of energies of groups of crystals (25 crystals in the EB, a varying number in EE), the so-called "trigger primitives", that are used in the CMS hardware triggering system. An extended description of the EB/EE can be found at [2]. Here we supplement this with a little detail on the ES.

The ES comprises 4 planes of silicon strip sensors and associated mechanics, cooling and front-end electronics. The sensors have an active area of 61×61 mm^2, divided into 32 strips. They are grouped into "ladders" of 7, 8 or 10 sensors. The planes are known as ES+F, ES+R, ES-F and ES-R, reflecting the nomenclature of the endcaps (+ or -) and whether the plane is "Front" (closest to the interaction point) or "Rear". The F planes have their strips aligned vertically and thus measure accurately the incidence position of electromagnetic showers in the horizontal direction. The opposite is true of the R planes. The ES front-end electronics can operate in two modes: High Gain ("HG") is used for calibration purposes and low-energy collision running; Low Gain (LG) has a higher dynamic range more suitable for higher energy collision runs.

2   ECAL Operation during LHC collisions

2.1   Crystal Calorimeter status and stability

Shortly after installation of the EB and EE, the percentage of working channels was 99.47% and 99.66% respectively, measured during cosmic-ray runs in late 2008 [2]. Some infant mortalities resulted in a slight decrease in these numbers, which is currently stable at 99.30% and 98.94%. In addition, a small number of channels, 0.3% in EB and 0.7% in EE, were classified as operable but problematic (e.g. high levels of electronic noise). These are suppressed in the offline reconstruction described in section 4.1. Figures 1 and 2 show maps of the EB and EE respectively, detailing the fully working areas and the few problematic channels. The energy deposited in channels with readout integrity problems can in principle be recovered by using the associated trigger primitive data. Only a small fraction of the total number of channels have neither readout nor trigger information available (0.1% of EB and 0.7% of EE). These regions are indicated by the white squares in figures 1 and 2.
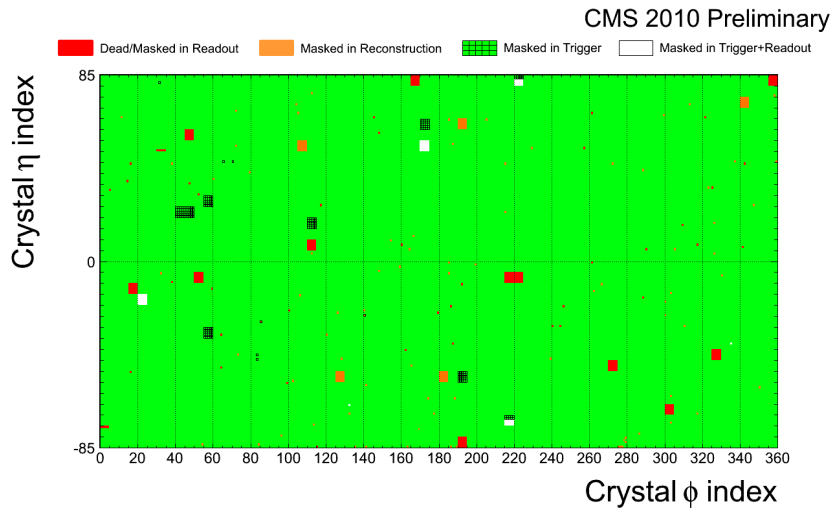

Figure 1: Graphical representation of the barrel ECAL (EB) showing the fully working areas (green) and few problematic channels. The percentage of fully operational channels in the EB is 99.30%.

2.1.1   Crystal transparency and thermal stability

One of the most challenging aspects of the CMS ECAL is achieving the required 0.5% constant term of the energy resolution for unconverted photons. Various factors contribute to this term, including the temperature stability of the crystals/photodetectors and the crystal transparency, which can decrease with radiation. It is thus crucial to ensure a stable thermal environment (specification for the EB/EE is a maximum variation of $0.05°C$ and $0.1°C$ respectively) and to monitor any changes in crystal transparency. To control the temperature an extensive feedback mechanism based on information from nearly 7000 thermistors is utilized. To monitor the radiation damage both LED and laser light monitoring systems are employed, which constantly monitor the transparency of the $PbWO_4$ crystals. Although radiation damage is not expected to be relevant until at least 2011, it is important that the light monitoring system itself is extremely stable, to better than 0.2% variation. Figure 3 (left) shows the stability of the thermistor measurements during the first two months of the 7 TeV data taking period in 2010, clearly meeting the specifications. Figure 3 (right) shows the measured ratio over time of the APD signal to that from a PN diode, when illuminated by the blue laser light of the monitoring system. The
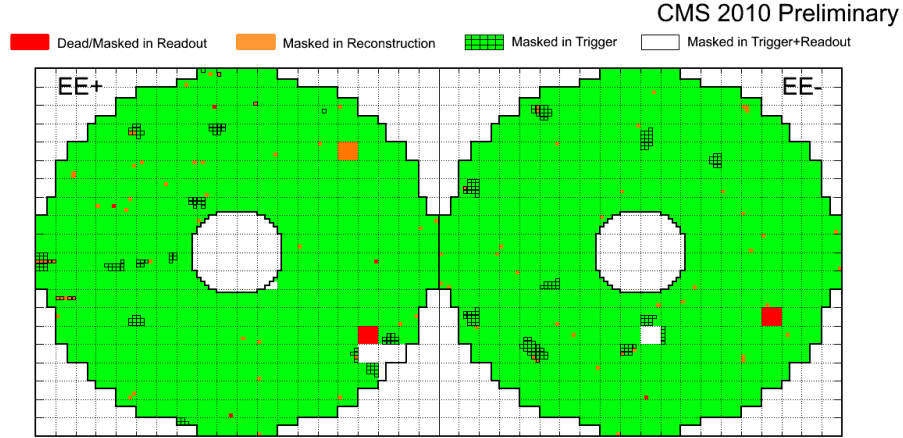
CMS 2010 Preliminary

Figure 2: Graphical representation of the endcap ECAL (EE) showing the fully working areas (green) and few problematic channels. The percentage of fully operational channels in the EE is 98.94%.

observed RMS variation of less than 0.03% shows that the stability is much better than that needed to achieve a constant term in the ECAL energy resolution of 0.5%.
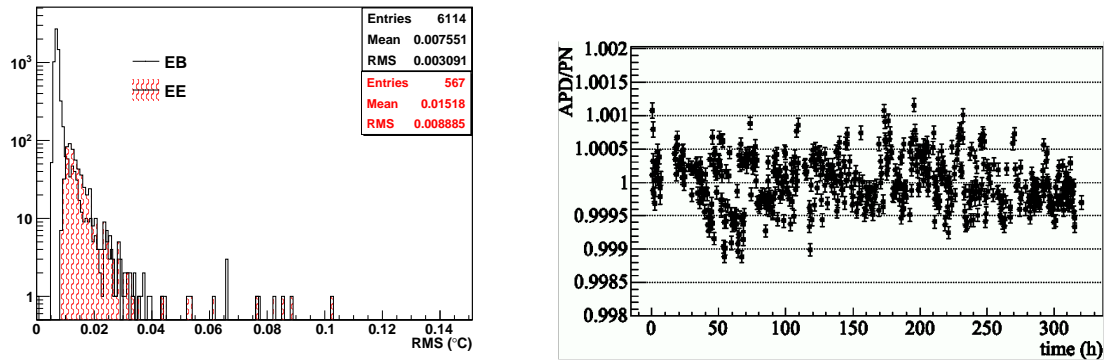

Figure 3: Left shows the temperature stability, represented by the rms of the measurements of each thermistor over two months. Right shows the measured signal stability over two weeks, represented by the ratio of signals from the APD and the PN diode when illuminated by the blue laser.

2.2 Preshower status

Of the 4288 silicon sensors forming the ES, 9 are classed as "dead" due to hardware problems that occurred after installation. In addition, a few strips (23 out of 137216 total) are classed as noisy. The total percentage of fully-functional strips is 99.79%. Figure 4 shows graphically the four ES planes, with the dead sensors marked as white squares and the noisy strips marked in red.

2.3 Timing Alignment

Reconstruction of the particle arrival times in EB/EE is obtained by comparing the digitized 25 ns spaced amplitude samples to the known shape of the scintillation-induced signal. The algorithm used in the EB/EE reconstruction employs ratios of consecutive samples [3]. The ES also records signal amplitudes every 25 ns but, in contrast to the 10 samples recorded by the EB/EE, only saves 3 consecutive samples per channel per trigger.
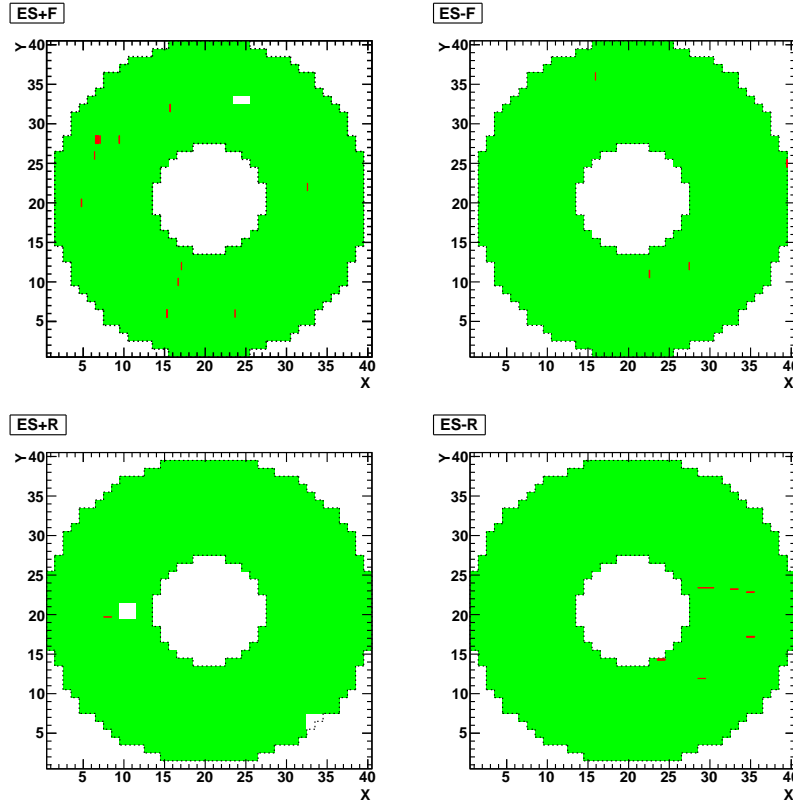
Figure 4: Graphical representation of the four ES planes, showing the dead sensors (white squares) and noisy strips (red strips). The percentage of fully operational channels in the ES is 99.79%.

The ECAL time measurement is defined such that a shower produced by a relativistic particle has *on average* a reconstructed time of 0 ns. To achieve this, a procedure of time alignment across all ECAL channels is necessary, which for EB and EE consists of two consecutive steps:

- **online alignment:** the read-out phase ("PLL phase") of the front-end electronics (common to 5×5 channels) is adjusted in steps of 1.04 ns to obtain, on average, the smallest possible reconstructed time.

- **offline alignment:** for each crystal, sub-nanosecond residual time mis-alignments are taken into account in the reconstruction.

Beam splash events[1] collected in the Autumn of 2009 were used to re-align the EB/EE readout time, with a procedure described in [3].

The impact of including offline time re-alignment for EB/EE is illustrated in figure 5, where the average time for hits above 0.6 GeV is shown for all barrel and endcap crystals in 7 TeV minimum bias events.

LHC collision data were then used to time-align individual regions of the EB/EE. The average reconstructed time for hits with energy above 2.5 GeV has been calculated for each of the two EE endcaps and for each of the 170 rings (of 360 crystals each) defined in the EB by constant pseudo-rapidity. This further reduced the spread of the times from about 0.3 ns to less than 40 ps, as demonstrated in figure 6, where the average reconstructed time is shown for each η

---

[1]Protons incident on collimators a few hundred metres from CMS produced a large spray of secondary particles - mostly muons - incident approximately uniformly over the calorimeters
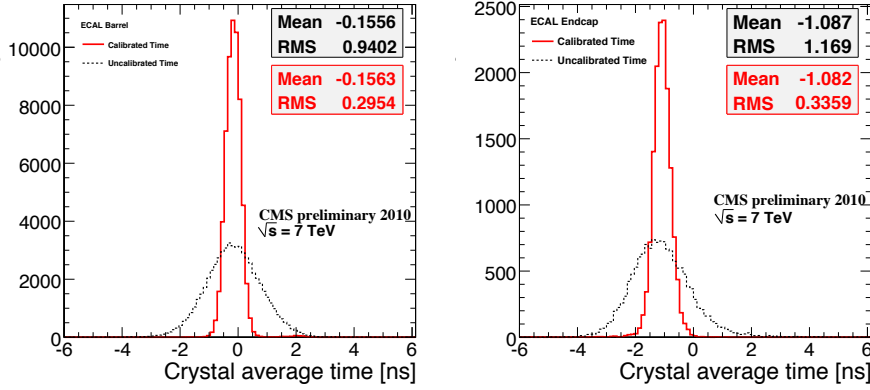
Figure 5: Mean time per EB/EE crystal hit after alignment of the online PLL readout phase alone (dashed) and the improvement of also including the offline time calibration from 2009 beam splashes (full).

ring, together with the projection of all rings.

The absolute time scale shows a deviation from zero of 50 ps, pointing to a shift between the calibration data set and several subsequent runs. Although the reasons for this effect are still being investigated, the timing precision is sufficient (sub-nanosecond) to be able to distinguish different pulse shapes (e.g. from anomalous signals - see section 4.2 - and some new physics) and provide accurate timing measurements for optimum trigger performance and background rejection.
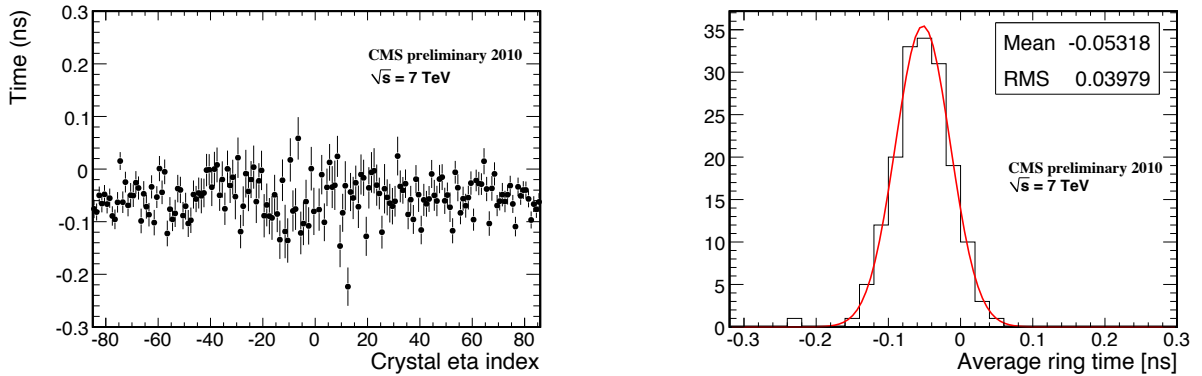

Figure 6: Mean reconstructed time for groups of 360 crystals belonging to rings at constant η, as a function of pseudo-rapidity (left) and for all rings (right). The collisions-obtained offline time alignments are applied in both cases.

The first step of ES time alignment was also the adjustment of the PLL digitization phase in steps of 1.04 ns, which in the ES case is common to a varying number of strips, between 192 and 300 depending on the ladder type. An initial estimation of the required ES PLL settings, based on the ES geometry and cable length, proved sufficiently accurate to be able to detect cosmic rays during the summer/autumn of 2009.

Collision data were then used to fine-tune the PLL phase adjustment for the whole ES. Figure 7 shows the synchronization of the relative phase for 7 TeV collision events, before and after fine-tuning of the PLLs. The width of the tuned distribution is around 0.3 ns, meaning that the reconstruction of energies from the three time samples can be performed in general by a simple weighting method (see section 4.1) rather than the more resource-intensive fitting of the
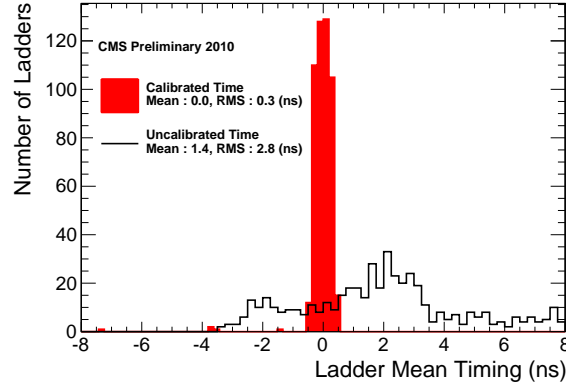
samples to an ideal pulse shape.

Figure 7: Synchronization of the relative phase between Preshower readout electronics (at the level of "ladders") and the passage of particles through the sensors, before and after fine-tuning.

2.4 Trigger

The EB/EE trigger systems were operational throughout the full period of 7 TeV data taking. The trigger algorithm is described in detail in [4] and [5]. The transverse energy for each trigger tower is summed to form the trigger primitive values. The minimum threshold used for triggering was 2 GeV for low beam intensity, subsequently increased to 5 GeV.

For each trigger tower additional measurements of the lateral extent of the energy deposition are made and included in the data stream as two digital bits.

The ECAL trigger must identify accurately the correct bunch-crossing ("BX") associated to signals in the EB/EE, as well as estimating the energy correctly. Timing scans were used to optimize the efficiency of the BX assignment, as shown in figure 8 (left). The rather wide plateau shows that the performance of the ECAL trigger is relatively insensitive to small (order of a nanosecond) jitters, either in the clock or due to offsets in the longitudinal primary vertex positions. Figure 8 (right) shows a comparison between the online trigger-primitive values and the offline measurements of tower transverse energies. The figure contains around 30 million entries and the remarkable agreement shows that the trigger is performing as expected. As can be seen in the figure, the maximum TP value is 64 GeV.
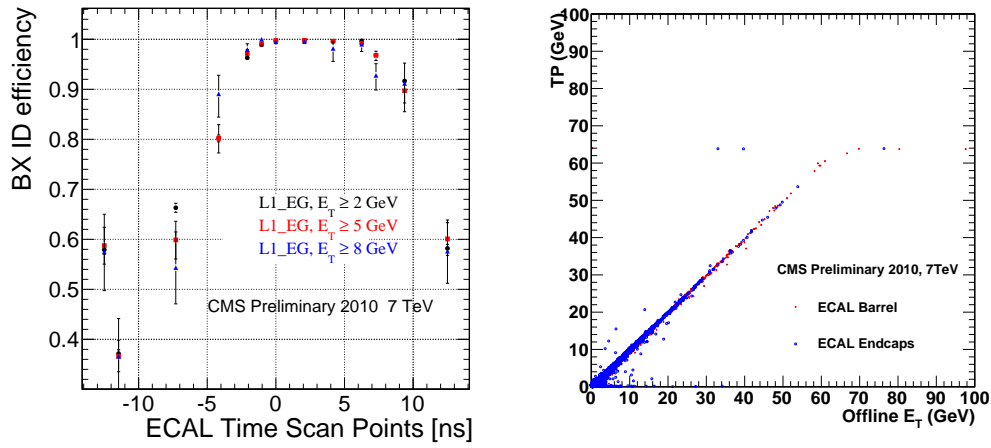
Figure 8: Left: Bunch-crossing (BX) assignment efficiency as a function of the time-setting used. Right: comparison between the online (TCC-computed) trigger primitives and offline measurements of the transverse energies contained in the towers. The plateau at TP = 64 GeV corresponds to the maximum hardware value.

3   Data sets and event selections

For this analysis, we select collision events triggered by a signal in any of the BSC scintillators coincident with a signal from either of the two BPTX detectors, indicating at least one bunch crossing at the interaction point (IP); these conditions are the same as those used in [6].

Offline, the conditions listed below were imposed, with the aim of selecting a sample with the largest possible acceptance whilst suppressing beam-related backgrounds.

- BPTX signals were required from both beams passing the IP in conjunction with a signal in either of the BSCs (the coincidence of the BSCs would have suppressed single diffraction signals);
- a primary vertex was required with $|z| < 15$ cm and a transverse distance from the z axis smaller than 2 cm; it was also required that at least three tracks be used in the vertex fitting and that at least NDF> 5;
- beam-halo event candidates were rejected; these events have hits in the BSCs with timing consistent with that of a particle traversing CMS horizontally;
- the fraction of high-quality tracks was required to be greater than 25%, for events with at least 10 reconstructed tracks. This cut aims at rejecting beam-scraping events, in which long horizontal sections of the pixel detector are hit;
- events were rejected if large signals consistent with noise in the HCAL were identified.

3.1   Monte-Carlo samples

The data are compared to simulated events obtained from the PYTHIA6 [7] event generator processed through a GEANT4 [8] simulation of the CMS detector. PYTHIA tune D6T is used in the following.

The position and width of the beam spot in the simulation were adjusted to those determined from the data. Simulated events were processed and reconstructed in the same manner as collision data.

Details on the simulation of the ECAL response, with modeling of the geometry and sensitive volumes, of the passage of particles through matter, of the readout electronics and of the tuning and validation of simulation parameters with test beam data are given elsewhere [9]. Latest improvements in the digitization step include the description of the variation of the individual channel gain, due to the variations in the crystal light yield and in the readout gain of the photodetectors, and the description of the correlation between noise in the different time samples. The former is described using the single channel intercalibration constants measured during the construction and commissioning phase of ECAL [2, 10]; the latter describes the average noise across the ECAL barrel and endcaps separately, with reference to in-situ measurements of the single sample noise [2] and their correlation. A detailed simulation of the digitization step and of the energy equivalent noise in each channel is important to account for the pileup, for the electron and photon isolation and for the jet description.

4 Offline reconstruction

4.1 Data reconstruction

The ECAL local reconstruction aims at the most accurate measurement of the energy of the particles impinging on the calorimeter as well as of their arrival time. Binary data from the off-detector readout electronics (Data Concentration Card - DCC for EB/EE, and ES-DCC for the Preshower) are decoded and their integrity checked. Possible errors are flagged in the header of the DCC/ES-DCC data and provided to the subsequent steps of the reconstruction, to undergo specific treatment whenever appropriate.

A digital filtering technique is applied to reconstruct the signal amplitudes in EB and EE starting from the availabe samples of the pulse shape digitized by the front-end electronics[11]. The signal time relative to a fixed readout phase is derived from the comparison of the time sample ratios to the expected pulse shape [3]. The amplitude and time reconstruction in the ES proceed similarly starting from the three available time samples.

The responses of the individual channels are equalized and synchronized by means of inter-calibration coefficients for the energy and timing measurements. These calibration constants, as well as the global energy scale conversion factors for EB, EE and ES, are retrieved from a database.

An electromagnetic shower spreads to more than one channel: for example, on average only about 70% of the energy of an unconverted photon impinging on the centre of an ECAL barrel crystal is contained within that crystal. For electrons and converted photons the energy deposition can be considerably spread along ϕ, due to the intense magnetic field of CMS. To achieve the best estimate of the energy of incoming particles, algorithms for clustering the energy deposits have been developed. Their optimization is different in EB and EE, to cope with the varying geometry. For the endcaps, EE cluster positions are extrapolated to the preshower and ES clusters built. The total endcap energy is a linear combination of cluster energies in the EE and ES. Further details on the clustering process are given in [12],[13].

During the reconstruction steps, known detector pathologies, mainly related to a few faulty or noisy channels (see Section 2), are handled by appropriate actions. Moreover, for each signal, quality flags are derived from the analysis of the pulse shape, of the signal time and of the pattern of the local energy deposits. This approach has proven effective in the treatment and cleaning of anomalous energy deposits (see below).

4.2 Cleaning of anomalous energy deposits

Algorithms have been developed to flag and reject isolated high energy deposits observed to occur in the ECAL barrel during collision data taking at 900 GeV, 2.36 TeV and 7 TeV centre-of-mass energies. These energy deposits are believed to be caused by direct ionization of the avalanche photodiode (APD) sensitive volumes by highly ionizing particles - mainly protons and heavy ions - produced during proton-proton collisions. Due to the fact that these deposits are observed in single crystals, they are often termed "spikes". The rate of these energy deposits is estimated to be approximately 1 in 10^3 minimum bias events. It is also observed to scale with $\sqrt{s}$ at a rate consistent with the measured increase in charged particle multiplicity [6]. The simulation of the direct ionization is under way but was not included in the MC code used for this analysis.

The anomalous energy deposits are flagged based on topological and timing characteristics. A topological variable comparing the energy in a single crystal, $E1$, to the summed energy in the

four adjacent crystals in η and ϕ, $E4$, is computed for each channel. This is known as the "Swiss Cross" variable. Figure 9(a) shows the distribution of the quantity $(1 - E4/E1)$ for data and simulation ($\sqrt{s} = 7$ TeV) for the channel with the highest reconstructed energy in each event. There is an excess of events in the data with $E_T > 3$ GeV and $(1 - E4/E1) \sim 1$, which is not present in the simulation. A cut of $(1 - E4/E1) < 0.95$ has a rejection power that depends on the signal transverse energy:

- 91.8% for $E_T > 3$ GeV.
- 97% for $E_T > 5$ GeV.
- 99.2% for $E_T > 10$ GeV.

Analysis of the signal pulse shape provides further discrimination between energy deposits from electromagnetic showers and those from direct ionization of the APD. The former are a convolution of the time profile of light emission from the lead tungstate crystals (80% of light emitted in 25 ns) and the response of the front-end electronics (shaping time $\tau \sim 40$ ns), whereas, for the latter, only the electronics shaping time contributes. This difference in shape produces a bias in the measured time of the signal pulse when the anomalous energy deposits are reconstructed with the expected pulse shape for scintillation light. Figure 9(b) shows the reconstructed time distribution for minimum bias data ($\sqrt{s} = 7$ TeV) for the channel with the highest reconstructed energy in each event. Signals produced by scintillation light are peaked at zero, whereas the apparent time of the anomalous signals is peaked at -10 ns due to the faster rise-time of their pulses. The long tail extending to $+60$ ns is believed to be due to non-prompt anomalous signals in the APD produced by low momentum neutrons, and the secondary peaks spaced at 25 ns intervals are an artifact of the sampling frequency of the front-end electronics.

For each reconstructed pulse, a flag is set based on the reconstructed time and the expected time resolution. A pulse is declared 'out-of-time' if the difference between the measured and expected time is greater than 5 standard deviations. Approximately 8% of anomalous signals with E_T greater than 3 GeV are non-isolated - they are flagged as out-of-time, but have $(1 - E4/E1) < 0.95$. These are indicated by the peak at -10 ns in the dashed histogram of figure 9(b).

For the analyses described in this note, anomalous energy deposits are removed by rejecting signals with E_T greater than 3 GeV and topological variable $(1 - E4/E1) > 0.95$.
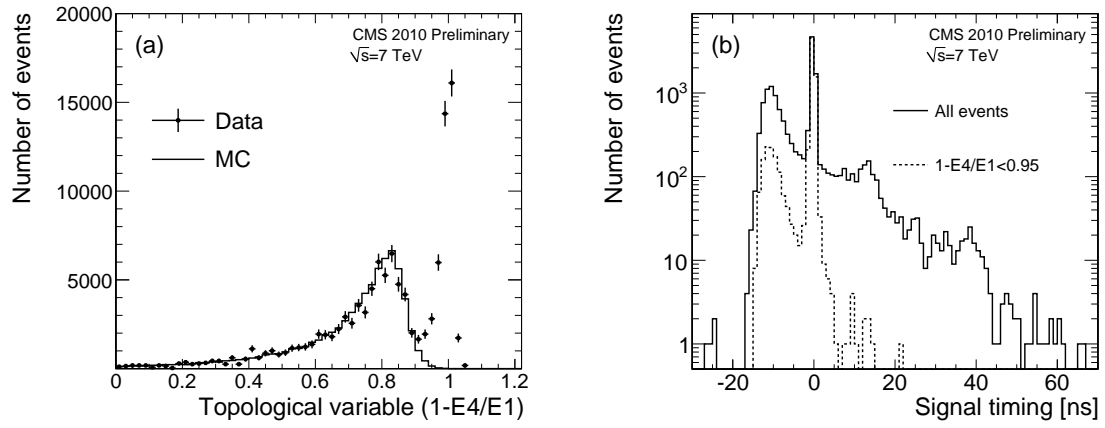
Figure 9: (a) Distribution of the "Swiss Cross" topological variable $(1 - E4/E1)$ for the highest energy deposit in each event for data and simulation ($\sqrt{s} = 7$ TeV). Only events with an energy deposit with $E_T > 3$ GeV are plotted. The two distributions are normalized to the same total number of minimum bias events, before the cut on the signal transverse energy is applied; (b) Reconstructed time corresponding to the maximum of the signal pulse for the highest energy deposit in each event (with $E_T > 3$ GeV). The dashed histogram indicates non-isolated energy deposits that satisfy $(1 - E4/E1) < 0.95$.

4.3   Data-MC comparisons of low level observables

Figure 10 shows the energy spectra of individual channels in the ECAL barrel and endcaps, normalized to the number of minimum bias triggers in data. Besides event quality selections, "spike" rejection cuts are applied only to the data since the spike events are not yet simulated in the MC.
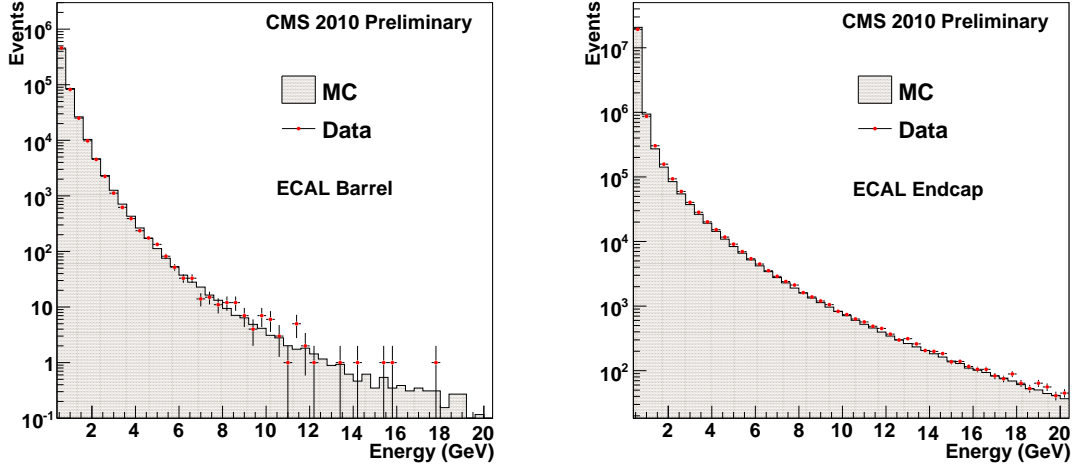

Figure 10: Energy spectra of the individual channels in the barrel (left) and in the endcaps (right) from 7 TeV minimum bias collision events.

The energy spectra for ES hits is shown in figure 11 for both data and Monte-Carlo, expressed as the number of "MIPs" - approximate number of minimum-ionizing particles traversing the silicon strips. The bump at high energy is due to the saturation of the read-out electronics, which were operating in High Gain. This saturation happens for each strip at a slightly different energy due to varying pedestals and gains, producing a bump rather than a single value. The simulation does reproduce this feature, although not yet perfectly.
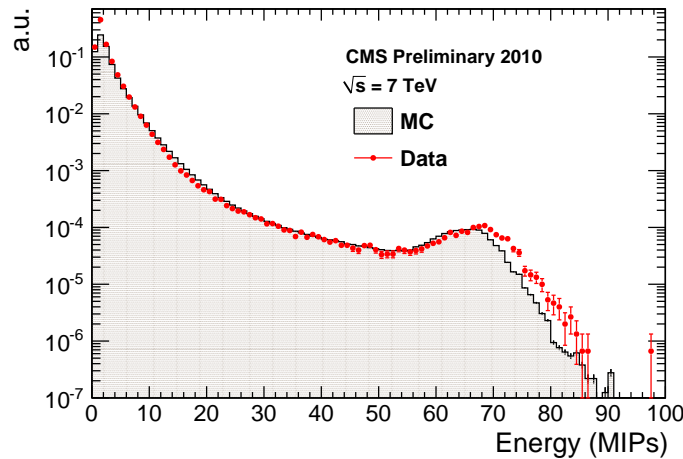

Figure 11: Energy spectra of the strips in the preshower from 7 TeV minimum bias collision events. The bump at high energy is due to signal saturation in High Gain mode.

The pseudo-rapidity distribution of the channel with the highest reconstructed energy in the barrel and in the two endcaps separately is presented in figures 12 and 13.
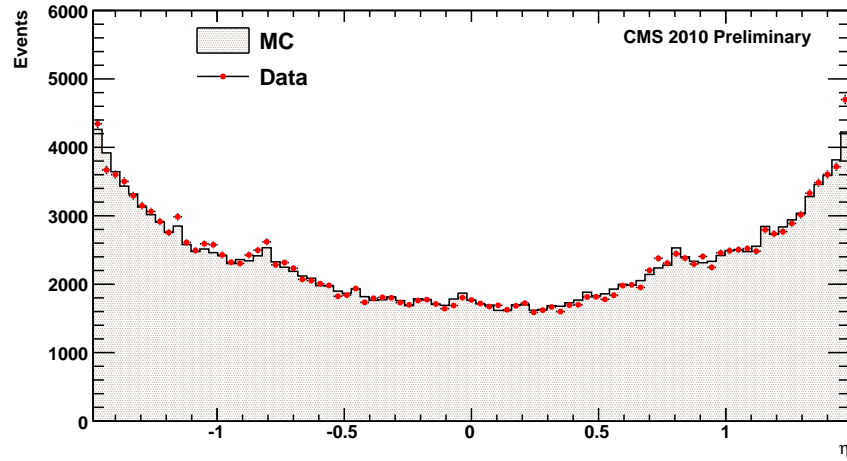
Figure 12: Pseudo-rapidity distributions of the channel with the highest reconstructed energy in 7 TeV minimum bias collision events for EB.
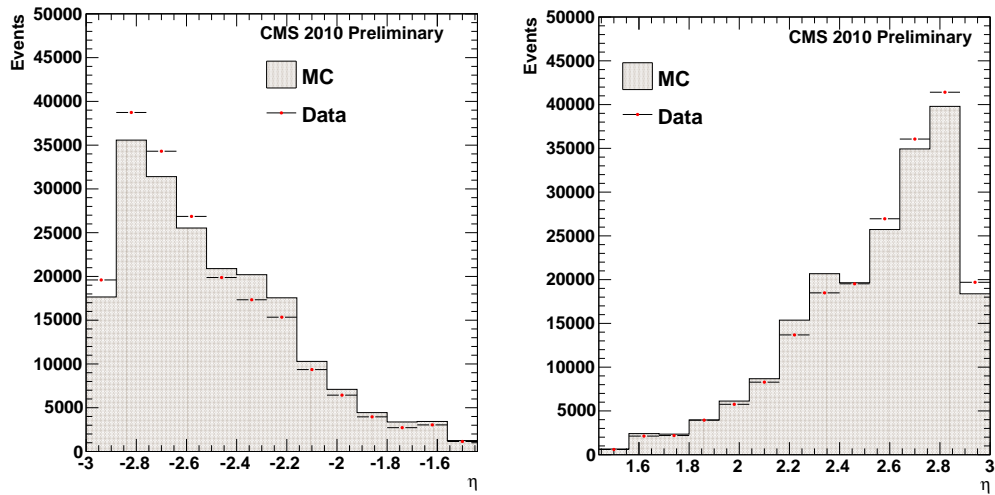

Figure 13: Pseudo-rapidity distributions of the channel with the highest reconstructed energy from 7 TeV minimum bias collision events for EE- (left) and EE+ (right).

Each of the three histograms contains one entry per event, to enhance the contribution of EB channels. A few channels with noise level higher than the average, not yet simulated in the MC, are excluded from the comparison in the endcaps. The difference between EE+ and EE- is related to the higher level of noise in EE-.

Figure 14 shows the azimuthal distribution of the maximum energy channel in the barrel and in the endcaps. Variations as a function of ϕ reflect the modularity and inhomogeneity of the energy equivalent noise in ECAL. Data and MC are normalized to the same number of selected minimum bias events. The detailed simulation of the digitization step and of the energy equivalent noise in each channel (see Sec.3.1) explains the excellent agreement between data and MC for the η and ϕ distributions.
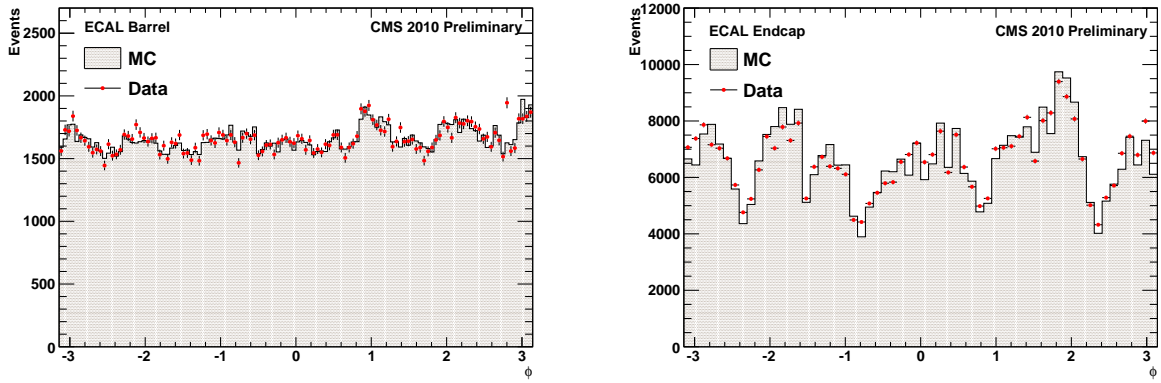

Figure 14: Azimuthal distribution of the channel in ECAL barrel (left) and ECAL endcaps (right) with the highest reconstructed energy from 7 TeV minimum bias collision events.

The ES occupancy is calculated as the percentage of strips with a reconstructed energy greater than four sigma of the noise. In HG mode this threshold corresponds to about 0.4 MIPs, or 32 keV of energy deposited in the strip. Figure 15(left) shows how the occupancy varies with pseudo-rapidity (averaged over all ϕ), whilst fig. 15(right) shows the variation with azimuthal angle (ϕ, averaged over all η), both compared with simulation, where absolute values of the MC occupancies have been normalized to the data. The ϕ variations are due to the X-Y geometry of the ES and are well-modeled by simulation.
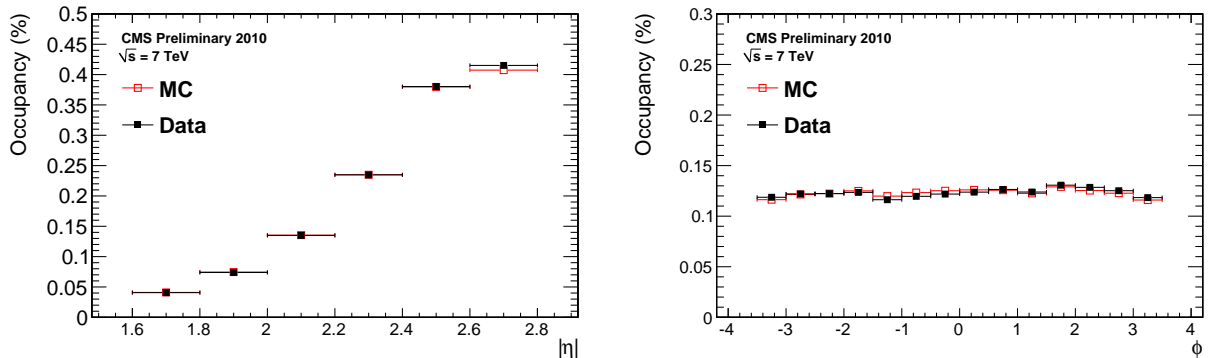

Figure 15: Preshower occupancy as functions of pseudo-rapidity (left, averaged over all ϕ)) and azimuthal angle (right, averaged over all η)

4.4 Data-MC comparisons of high level observables

To achieve the best estimate of the energy of incoming particles, algorithms for clustering the energy deposits have been developed. This is done in two steps for the barrel and three for the endcaps.

- Firstly, in both EB and EE, "basic clusters" (BC) of groups of crystals are formed around seed crystals having $E_T >$1 GeV.

- Then, for the endcaps, BC positions are extrapolated to the preshower and geometrically-matching ES clusters built. The ES energy in MIPs is then converted to GeV and added to the EE BC energy.

- The barrel and endcap clusters are then further grouped, into "superclusters" (SC), which are extended in ϕ, thus minimizing the cluster containment variations due to the strong magnetic field. The optimization of the clustering is different in EB and EE, to cope with the varying geometry.

Figure 16 shows the ES cluster energies for each plane for 7 TeV minimum bias events, for both data and MC.
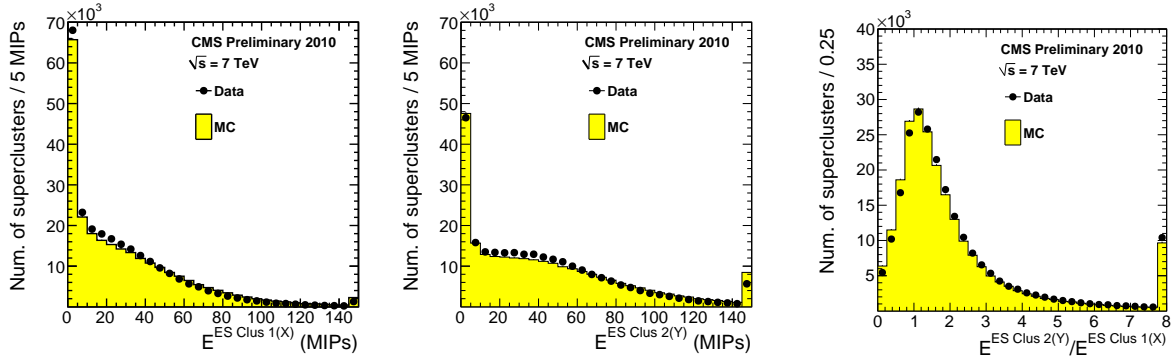

Figure 16: Comparison between data and simulation for the total cluster energies measured by each plane of the ES, expressed in units of MIP, as well as the ratio between the energies.

The ES cluster energies in each plane are weighted to give a total ES energy, as:

$$E_{EStot} = E^{ESClus1(X)} + 0.7 \times E^{ESClus2(Y)} \tag{1}$$

where $E^{ESClus1(X)}$ and $E^{ESClus2(Y)}$ are the summed cluster energies in each preshower plane.

Figure 17 shows the correspondence between EE basic cluster energies and associated ES clusters, for both data and MC, for electron candidates without any identification requirement and with energy measured by the combination of the silicon tracker and ECAL[2] between 70 GeV and 75 GeV. This correspondence is used to re-calibrate the energy measured in the EE with that in the ES, as described in [14]. Other 5 GeV-wide energy bands were used to check that the calibration coefficient (-0.025 GeV/MIP) is constant for electrons with energies between 60 GeV and 130 GeV.

Figure 18 shows the distribution of 'raw' transverse energy (meaning calculated from uncorrected energy) for superclusters in both barrel and endcaps.

These distributions show good agreement between data and simulation, demonstrating the maturity of the understanding of the detector and reconstruction algorithms.

---

[2]The ECAL energy is estimated using the EE energy plus the ES energy weighted using an estimate of the MIP$\longrightarrow$GeV conversion coefficient obtained from beam tests
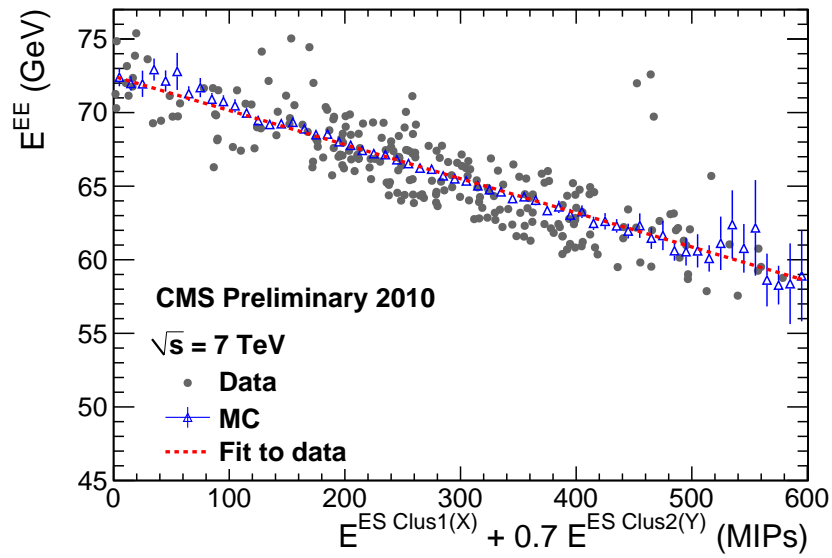
Figure 17: Correspondence between the energy measured in EE basic clusters and the weighted ES energy for electrons with energies between 70 and 75 GeV. For the data, one point represents a single electron, whilst for the MC we use a profile plot due to the larger available statistics.
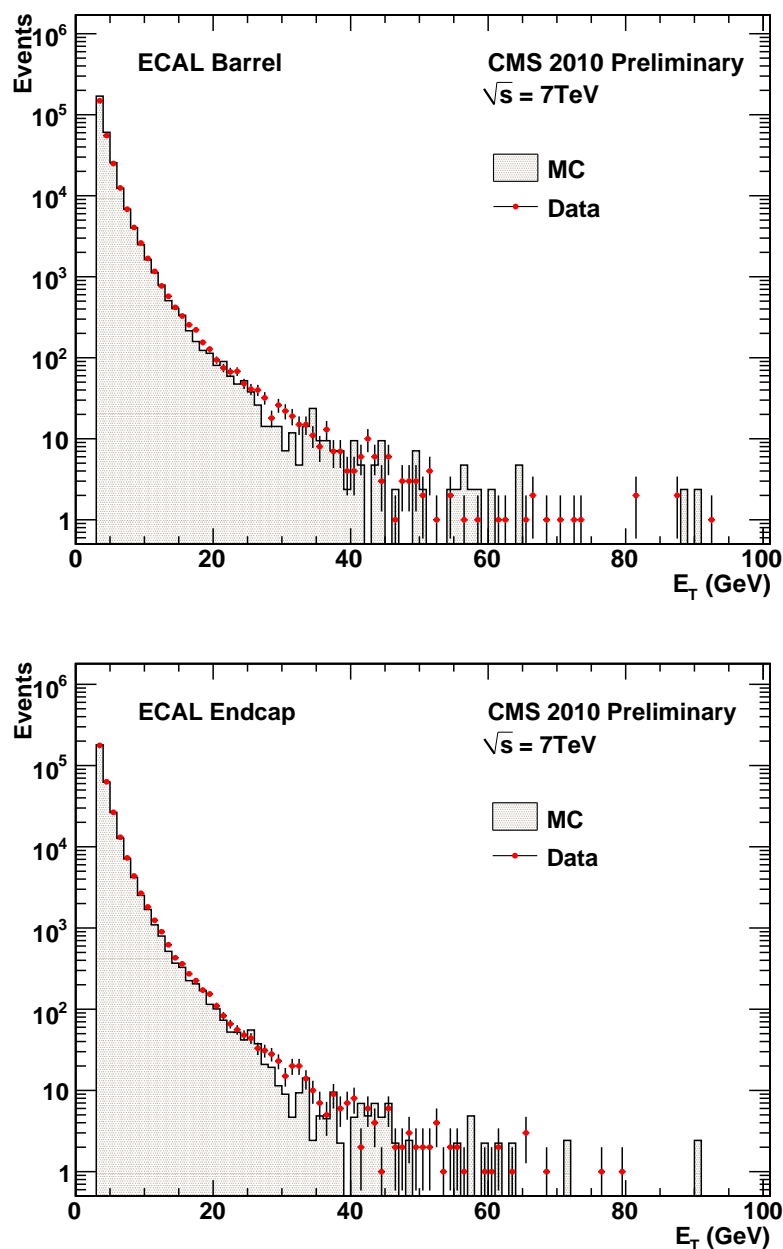
Figure 18: Transverse energy spectra for EB (top) and EE (bottom) superclusters from 7 TeV minimum bias collision events.

5   Performance results

5.1   Timing performance

In EB/EE the single channel time resolution can be parameterized as a quadratic sum of three terms, each accounting for a different source of uncertainty:

$$\sigma^2(t) = \left(\frac{N\sigma_n}{A}\right)^2 + \left(\frac{S}{\sqrt{A}}\right)^2 + C^2 \tag{2}$$

where:

- A is the measured amplitude in ADC counts;
- σ_n is the noise of the ten digitized ECAL samples;
- N is the *noise* term, due to the electronic noise affecting each of the digitised samples and to the procedure of pedestal subtraction;
- S is the *stochastic* term, arising from the photon collection time fluctuations, which has been demonstrated to be negligible [3];
- C is the *constant* term ascribed to systematic effects such as the slight differences between the signal shapes of each channel and the finite precision of the time-alignment procedure.

A measurement of the time resolution is extracted from the distribution of time differences between neighbouring crystals inside a cluster. In bins of A_{eff}, such distributions are described by a Gaussian whose width is parameterized by:

$$\sigma^2(t_2 - t_1) = \left(\frac{N\sigma_n}{A_{eff}}\right)^2 + 2C^2 \tag{3}$$

where $A_{eff} = A_1 A_2 \sqrt{A_1^2 + A_2^2}$.

Using collision events, $\sigma^2(t_2 - t_1)$ as a function of A_{eff} is shown in Figure 19. The fitted values of the *noise* term, 27.45 ± 0.29 ns and 36.08 ± 0.32 ns for EB and EE respectively, are consistent with expectations from test beam data and measurements made during CRAFT08 [3].

The *constant* term is estimated to be 0.27 ± 0.03 ns for EB and 0.18 ± 0.04 ns for both EE. They indicate the time measurement precision achievable by a single EB/EE channel for high energy deposits.
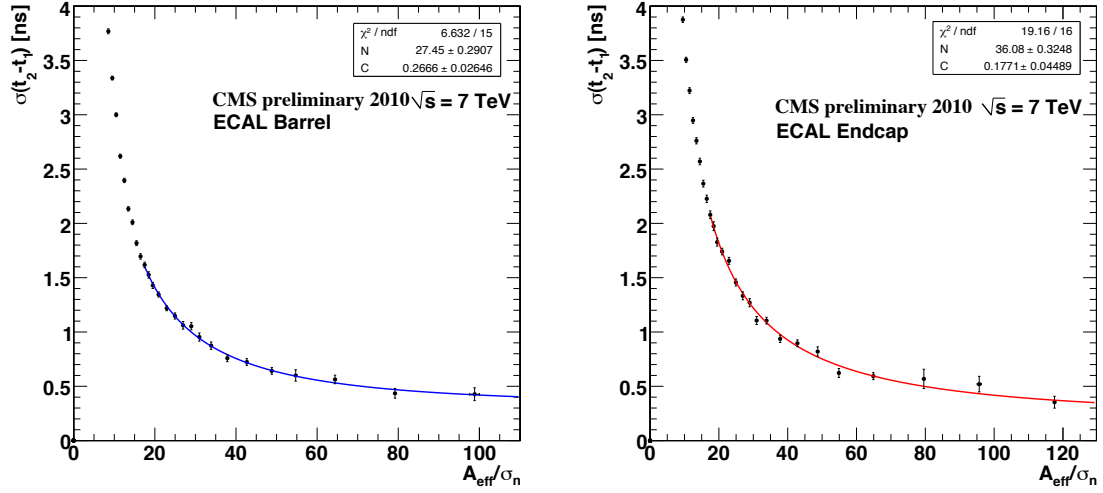
Figure 19: Gaussian width of the time difference between two neighbouring crystals as a function of the variable A_{eff}/σ_N, for EB (left) and EE (right). The fitted curves are shown as continuous lines. Energies range, respectively, up to 4.5 GeV and 18 GeV.

5.2   Geometrical Alignment

In this section we report on studies regarding the relative position of the EE and ES with respect to the tracker.

Similar studies for the EB indicate a possible small displacement, compatible with the optical survey results, of about 5 mm. Increased integrated luminosity will provide more high momentum charged tracks with which to make a more detailed study.

5.2.1   Alignment between Tracker and EE/ES

As the tracker and endcap disks (supporting the EE and ES) are independent objects there is a non-negligible probability of mis-alignment between them. A relative alignment can be performed using charged tracks coming from the interaction point.

As the ES was operated in HG mode it was sensitive to the passage of single charged particles, albeit with limited position accuracy of about 550 μm[3]. High purity tracks were selected, with at least 10 tracker hits (including one in the outermost layer) and $p_T > 1.5$ GeV/c, resulting in an extrapolation error of less than 1 cm. Cuts were also made on the track direction ($1.7 < |\eta| < 2.3$) and the few dead areas of the ES were not used.

A "stepping helix" track propagator was used to predict the position of hits on the ES sensors in each plane and a search window 30 mm wide was opened. The position of the found hit was set to be the centre of the strip.

The position of the ES hits were compared to the prediction from the tracker and residuals calculated. An iterative procedure was then used to determine the optimum alignment parameters, allowing the ES planes to float in X, Y and Z directions. Figure 20 shows the residuals for each ES plane, both before and after software alignment. They show that there is a relative mis-alignment in the vertical positions of the Tracker with respect of both ES endcaps (shown by the ES+R and ES-R planes) of about 8 mm[4] and a horizontal mis-alignment between the Tracker and the positive ES endcap of about 5 mm.

5.2.2   Alignment between ES and EE

The ES disks are supported by a conical structure attached to the backplate of the endcap hadron calorimeters (HEs). This backplate also supports the EE Dees, so relative alignment between the EE and ES should be rather good by design. EE clusters with $E_T > 2$ GeV, with no isolation or electron/photon identification requirements, were used as the source of this study, with position measurements being made in the EE and the ES. Note that the accuracy of these position measurements is rather poor due to the low E_T of a majority of the superclusters, but is sufficient for a first alignment. The same study was made with MC, assuming perfect alignment. Figure 21 shows the alignment between the EE and ES. The "out of the box" mis-alignment is less than half a millimetre in all planes.

---

[3]This corresponds to about 1.9 mm/$\sqrt{12}$

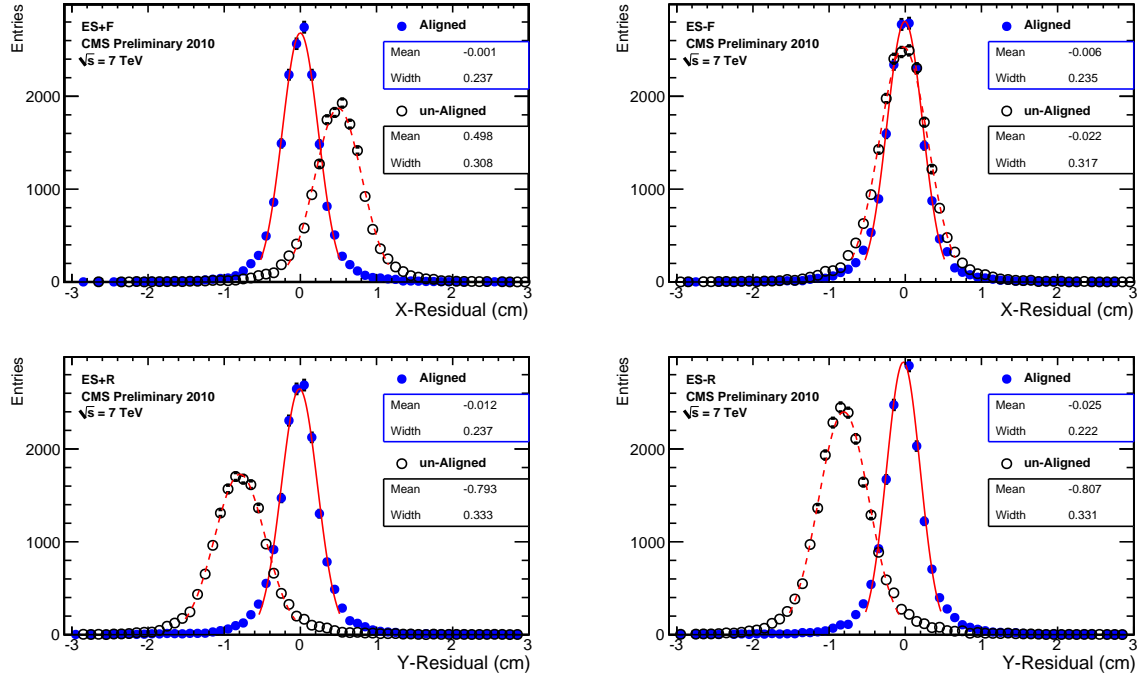[4]The tracker is 8 mm too low with respect to the ES endcaps

Figure 20: Residual measurements between Tracker and each of the ES planes, before and after software alignment.
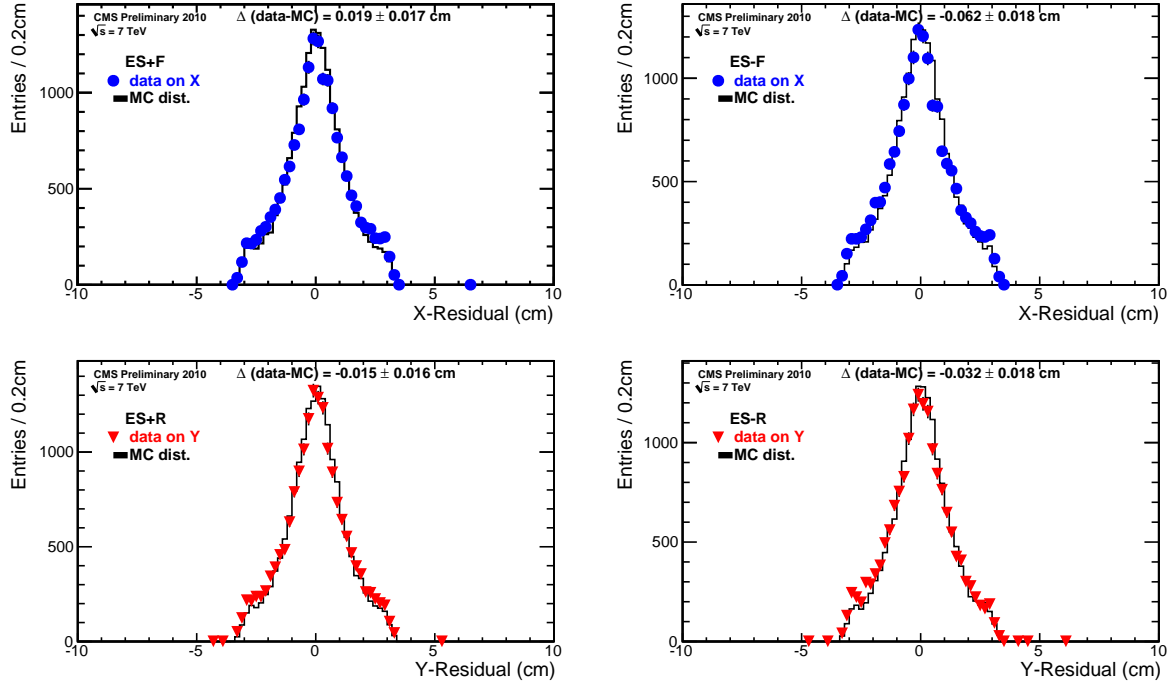

Figure 21: Alignment between ES and EE for each ES plane, for both data and MC. The "out of the box" alignment is better than a millimetre.

5.2.3 Alignment between EE and tracker

Finally, to study the EE alignment with respect of the tracker, superclusters were matched to charged tracks and the difference in pseudo-rapidity between the EE supercluster and the track calculated:

$$\Delta\eta = \eta(EE_{SC}) - \eta(trk).$$

The results are shown as darker (black) crosses in figure 22 as a function of azimuthal angle (ϕ).

The displacement is maximum at $\pm\pi/2$, i.e., along the y axis. This confirms the measured ES-tracker misalignment measurements of about 7-8 mm in the vertical direction.

Note that due its definition, a negative value of $\Delta\eta$ for EE+ has the same geometrical meaning as a positive value for EE-.
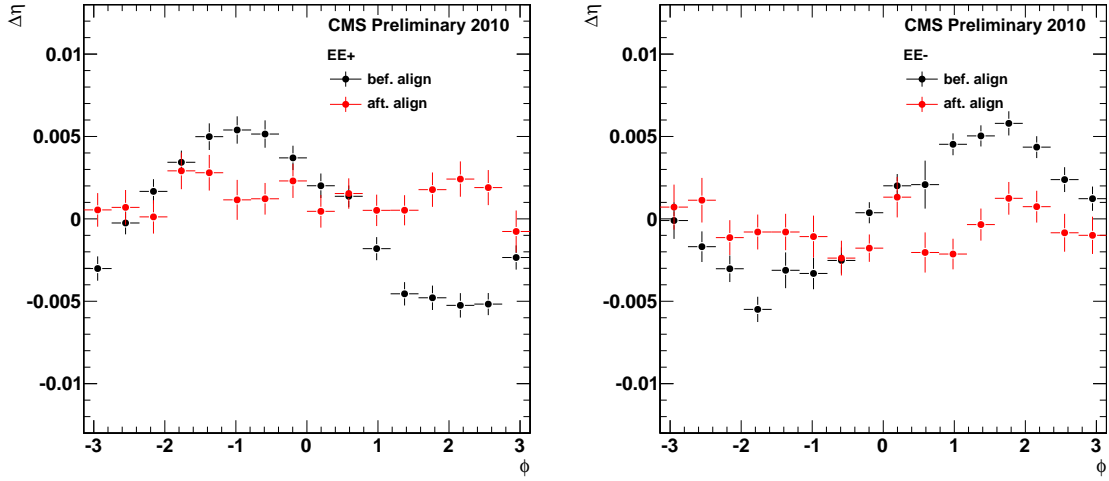

Figure 22: Alignment between Tracker and EE+ (left) and EE- (right) before and after software re-alignment.

Using the results from the ES-tracker analysis, the positions of the endcaps were changed in the software. The results are shown in figure 22 as lighter (red) crosses.

5.3 Preshower performance

5.3.1 Signal-to-noise for single ionizing particles

After in-situ calibration (see [14]) and measurement of the noise of each channel, an estimation of the signal to noise for single ionizing particles can be made. The design specification of the ES was to have an S/N ratio for single particles of about 8 for HG mode. The observed ratio, as shown in figure 23(left) is between 9 and 11.

5.3.2 Hit efficiency

The hit-matching efficiency is defined as the probability of finding a hit in the ES within a window around extrapolations of charged tracks from the primary vertex. The measured efficiency is actually a convolution of the efficiencies of the tracking, the extrapolation to the ES and the ES itself. Figure 23(right) shows this efficiency, averaged over all four ES planes, as a function of track p_T for 7 TeV minimum bias collision data and simulation. The p_T dependence is due to impurity of the track reconstruction algorithm - mainly fake tracks. The real ES efficiency for $p_T > 7$ GeV is, in the simulation, 100%. The agreement between data and MC demonstrates that the plateau below 100% in figure 23 is indeed due to inefficiencies in the track extrapolation.
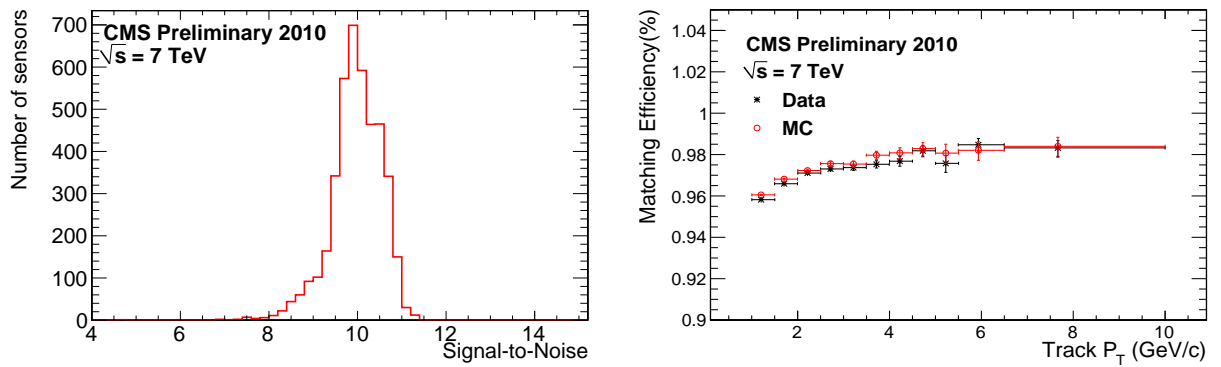

Figure 23: Preshower signal to noise ratio for single particles (left) and matching efficiency (right). The matching efficiency decreases for low p_T due to multiple scattering, whilst the plateau is not at 100% due to fake tracks etc.

5.4 EB energy resolution

In the absence of significant samples of high energy photons/electrons, we use reconstructed π^0 candidates in data (see section 5.5) to study the EB energy resolution. Figure 24 illustrates the resolution of the $\gamma\gamma$ invariant mass as a function of the candidate's η and transverse momentum p_T for data and MC, showing a good agreement.

We use the MC truth information to separate the contribution of the angular and energy resolutions to the measured invariant mass resolution. For each reconstructed photon pair:

- each photon candidate is matched to an MC-truth photon within a cone of $\Delta R = 0.1$ and only pairs with both legs successfully matched are retained;
- the opening angle Θ_{MC} between the MC-truth photons is computed;

and then either of the following is performed:

- the reconstructed opening angle Θ_{reco} is replaced by the true opening angle Θ_{MC} and the invariant mass $m_{\gamma\gamma}$ is recomputed as $m_{\gamma\gamma} = \sqrt{2E_1E_2(1 - \cos\Theta_{MC})}$;
- the invariant mass is recomputed by using the true energy for each photon candidate while keeping the reconstructed opening angle.

The mass resolutions using the true energy or true opening angle are also shown in figure 24 (bottom) in order to determine the dominant factors. Indeed it can be seen that the mass resolution is dominated by the uncertainty on the energy value for $p_T \leq 4$ GeV while at higher transverse momentum, $p_T > 4$ GeV, the angular resolution becomes the dominant source of error.
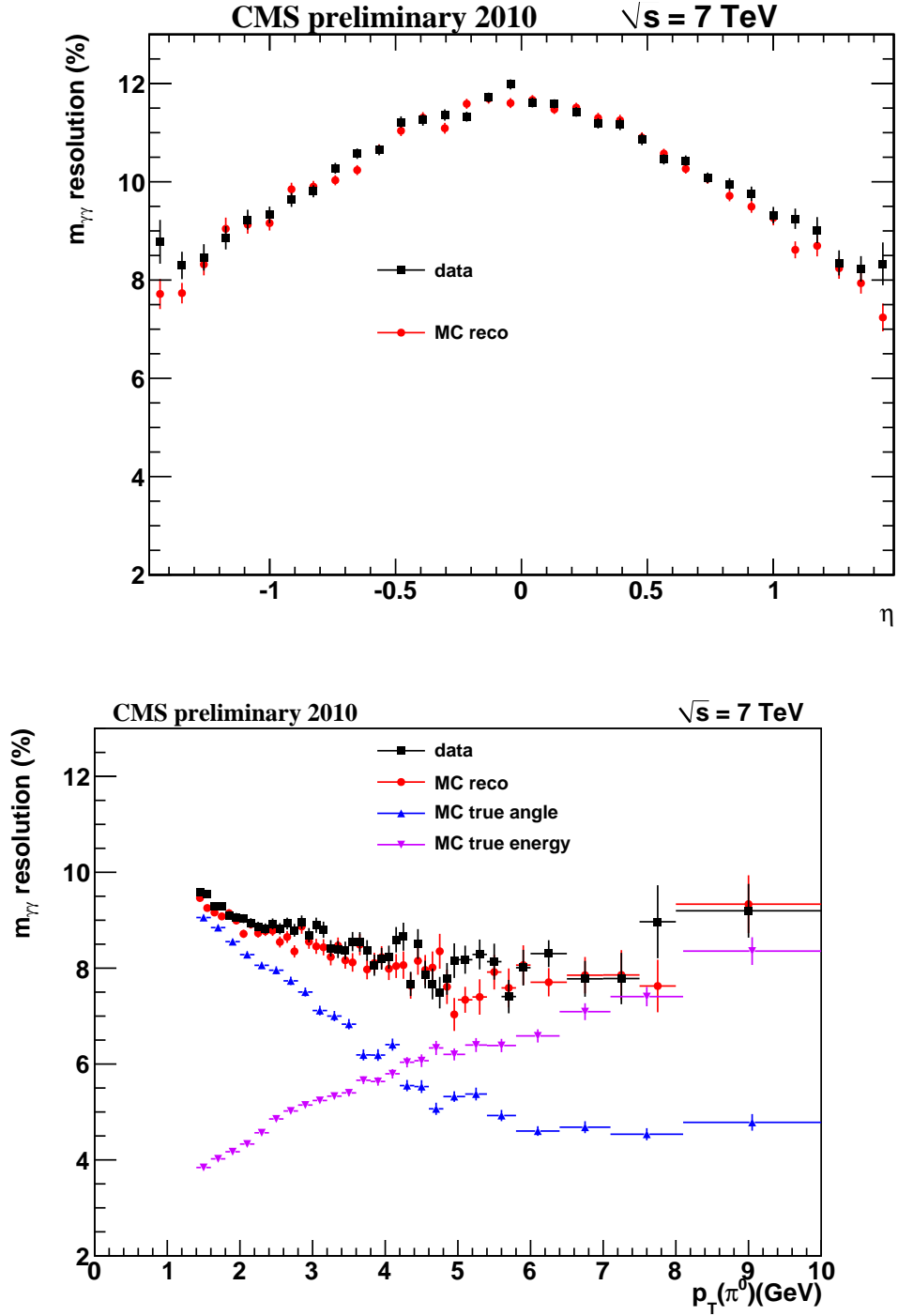
Figure 24: Resolution of the $\gamma\gamma$ invariant mass as a function of η (top) and p_T (bottom) of the $\gamma\gamma$ pair. For the top plot we have used mainly low p_T information. In the lower plot we include plots of the simulated mass resolution obtained when using either the MC true energy or MC true angle, to determine the dominant factors.

5.5 Neutral pion mass distribution stability with time

The first resonance observed in CMS was the π^0, demonstrating that the performance of the ECAL, even with extremely low mass objects, is excellent. Figure 25 shows the reconstructed photon-pair mass spectrum, including the π^0 peak.
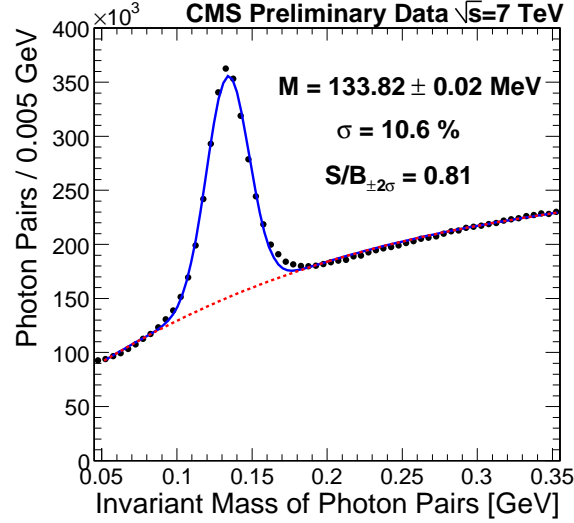

Figure 25: Mass spectrum of reconstructed pairs of photons showing a clear peak corresponding to the π^0 mass.

The measured mass of the π^0 is sensitive to the stability of the ECAL with time, from effects such as those described previously in section 2.1. Figure 26 shows the mass measurement variation as a function of time for the first 7 weeks of 7 TeV operation. Only relatively long runs with more than 10k reconstructed π^0 candidates were used, in order to reduce the statistical errors on the mass measurements to less than 0.2%. The stability of the mass measurements is around 0.14%.
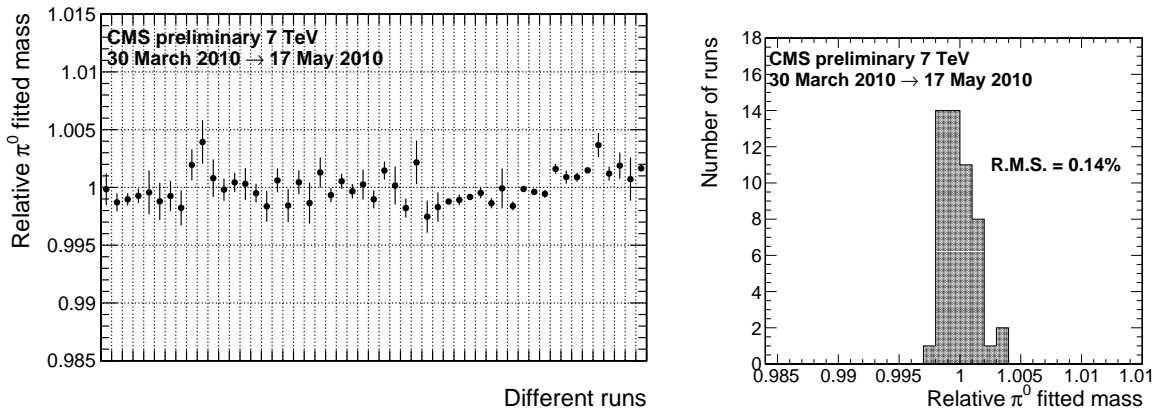

Figure 26: Stability of the measurement of the π^0 mass peak in the barrel ECAL. Left plot shows the mass peak as a function of run number, whilst the right plot is the projection, showing an RMS variation of around 0.18%

6 Conclusions

Throughout the first data taking periods of the LHC, the CMS ECAL has been operational, providing both data and trigger information. The stability of all components is excellent in these early stages and is being constantly monitored. The first collisions at 7 TeV have provided the opportunity to tune the detector (in terms of timing etc.) and to test our understanding of the basic observables, such as energy distributions, clustering etc. Good agreement between data and simulation has been shown for all observables, demonstrating an excellent understanding of the ECAL *in-situ*.

References

[1] CMS Collaboration, "The CMS experiment at the CERN LHC", *Journal of Instrumentation* **0803** (2008) S08004. `doi:10.1088/1748-0221/3/08/S08004`.

[2] CMS Collaboration, "Performance and operation of the CMS electromagnetic calorimeter", *Journal of Instrumentation* **5** (2010) T03010. `doi:10.1088/1748-0221/5/03/T03010`.

[3] CMS Collaboration, "Time reconstruction and performance of the CMS electromagnetic calorimeter", *Journal of Instrumentation* **5** (2010) T03011. `doi:10.1088/1748-0221/5/03/T03011`.

[4] P. Paganini, "CMS Electromagnetic Trigger commissioning and first operation experiences", *J. Phys. Conf. Ser.* **160** (2009) 012062. `doi:10.1088/1742-6596/160/1/012062`.

[5] CMS Collaboration, "Performance of the CMS Level-1 Trigger during Commissioning with Cosmic Ray Muons", *Journal of Instrumentation* **5** (2010) T03002. `doi:10.1088/1748-0221/5/03/T03002`.

[6] V. Khachatryan, A. M. Sirunyan, A. Tumasyan et al., "Transverse-Momentum and Pseudorapidity Distributions of Charged Hadrons in pp Collisions at $\sqrt{s} = 7$ TeV", *Phys. Rev. Lett.* **105** (Jul, 2010) 022002. `doi:10.1103/PhysRevLett.105.022002`.

[7] T. Sjostrand, S. Mrenna, and P. Skands, "PYTHIA 6.4 physics and manual", *JHEP* **0605** (2006) 026.

[8] S. Agostinelli et al., "GEANT4: A simulation toolkit", *Nucl. Instrum. Meth. A* **506** (2003) 250.

[9] F. Cossutti, "The simulation of the CMS electromagnetic calorimeter", *CMS Conference Report* **CMS-CR 2007/043** (2007).

[10] P. Adzic et al., "Intercalibration of the barrel electromagnetic calorimeter of the CMS experiment at start-up", *Journal of Instrumentation* **3** (2008) P10007.

[11] P. Adzic et al., "Reconstruction of the signal amplitude of the CMS electromagnetic calorimeter", *Euro. Phys. Journal C* **46, Supplement 1** (2006) 23–35. `doi:10.1140/epjcd/s2006-02-002-x`.

[12] CMS Collaboration, "CMS ECAL Technical Design Report", *CERN/LHCC 97-33* (1997).

[13] CMS Collaboration, "CMS Physics TDR: Volume I (PTDR1), Detector Performance and Software", *CERN/LHCC-2006-001* (2006).

[14] CMS Collaboration, "Electromagnetic calorimeter calibration with 7 TeV data", *PAS* **EGM-10-003** (2010).